Modeling deformation and chaining of flexible shells in a nematic solvent with finite elements on an adaptive moving mesh

Andrew DeBenedictis, Timothy J. Atherton, Andrea L. Rodarte, and Linda S. Hirst

Phys. Rev. E **97**, 032701 — Published 2 March 2018

DOI: 10.1103/PhysRevE.97.032701

Modeling deformation and chaining of flexible shells in a nematic solvent with finite elements on an adaptive moving mesh

Andrew DeBenedictis and Timothy J. Atherton*
Department of Physics and Astronomy, Tufts University, 574 Boston Avenue, Medford, Massachusetts 02155, USA

Andrea L. Rodarte and Linda S. Hirst
Department of Physics, University of California, Merced, 5200 Lake Road, Merced, California 95343, USA

A micrometer-scale elastic shell immersed in a nematic liquid crystal may be deformed by the host if the cost of deformation is comparable to the cost of elastic deformation of the nematic. Moreover, such inclusions interact and form chains due to quadrupolar distortions induced in the host. A continuum theory model using finite elements is developed for this system, using mesh regularization and dynamic refinement to ensure quality of the numerical representation even for large deformations. From this model, we determine the influence of the shell elasticity, nematic elasticity and anchoring condition on the shape of the shell and hence extract parameter values from an experimental realization. Extending the model to multi-body interactions, we predict the alignment angle of the chain with respect to the host nematic as a function of aspect ratio, which is found to be in excellent agreement with experiments.

I. INTRODUCTION

An important application of nematic liquid crystals (LCs) is as guides for self assembly of included colloidal particles [1–4]. Chemical treatment of the particles may induce a preferred orientation of the adjacent nematic on their surface and induce elastic distortions in the bulk liquid crystal. Elasticity-mediated interactions between particles cause micron-sized particles to self-organize into chains or clusters that are strongly ($\sim 1000 k_B T$) bound together [2, 5–7]. Smaller nanoparticles (NPs) disperse uniformly in the isotropic phase but can be sculpted into a variety of structures by kinetic effects as the host undergoes a transition into a liquid crystalline phase [1, 8, 9]. Self-assembly of nanoparticles in LCs can therefore exploit nucleation and growth as would occur in an isotropic fluid [10, 11], but the liquid crystalline order permits additional control over the self-assembled structure [9].

Hierarchical structures can be formed by combining these mechanisms. Two co-authors of this paper (Rodarte, Hirst) created nanoparticle shells [12] by cooling a solution of mesogen-functionalized quantum dots in 5CB from the isotropic to nematic phase. The nanoparticles are driven to the boundary of the vanishing isotropic phase and by a nucleating inner nematic domain; they aggregate and solidify, leaving behind a shell. As shown in Fig. 1, shells then migrate to align in long chains due to the elastic interactions and adopt a more elongated morphology over time.

In this paper, we develop a model of the elongation and chaining process by minimizing the elastic free energy with respect to both the spatially varying orientation of the liquid crystal *and* the shape of the shell. We predict the LC orientation and the shell shape as a function of the elastic constants, and determine the orientation of the chains with respect to the bulk nematic. Results are compared with experiment and earlier models that neglect the shape of the particles [6, 13] or use perfectly ellipsoidal particles [14].

Shape-order optimization problems such as the shells in this paper are challenging because few analytical results are available and computational approaches must maintain the quality of the numerical representation during optimization. However, the ability to solve such problems may provide insight into the origins of complex shapes observed in biological systems [15]. A related and widely studied problem is to determine the shape of a *tactoid*, a droplet of nematic liquid crystal in a host solvent. While a variety of tactoid shapes is observed in lyotropic systems [16–18], including some that are not simply-connected [19, 20] and others that respond to temperature changes [21], thermotropic liquid crystals such as 5CB generally form spherical droplets because the surface tension between the LC and host tends to be much larger than the cost of elastic deformations.

For the shells in [12] and considered here, significant deformation occurs because the surface in question is not the interface between the LC and a host fluid but rather the surface of the thin shell that is surrounded inside and out by the LC. Similar deformations—including elongation and cusp formation— appear when lipid vesicles are embedded in a nematic host[22–24], and also in shells of active nematic whre defects template the formation of long spindle structures that appear and disappear in well-defined oscillations [25].

Migration of objects in a host nematic to form chains has been studied previously with colloidal glass spheres [2, 26, 27]. These authors observe alignment angles of $\sim 30^\circ$ for particles that produce a quadrupolar distortion

* timothy.atherton@tufts.edu

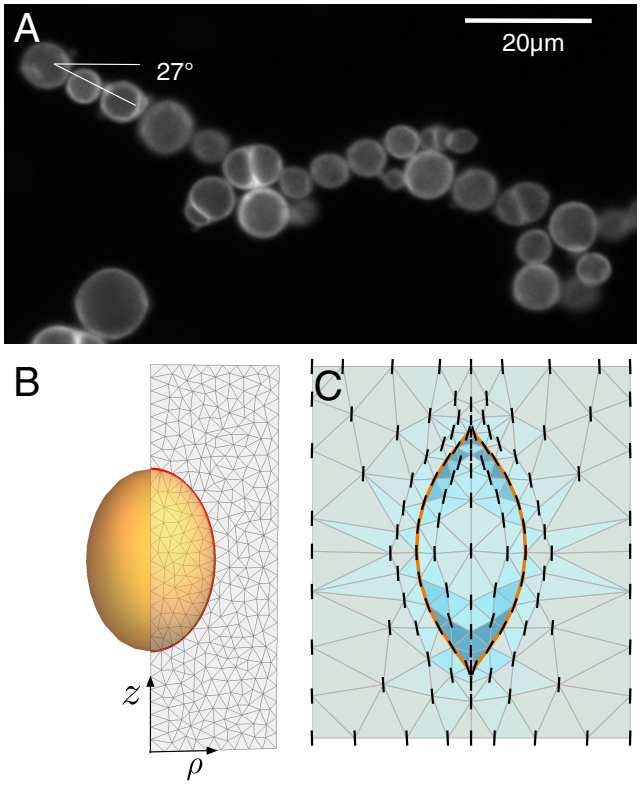

Figure 1. **A** Fluorescence microscopy images of quantum dot microshells [12] show subtly elongated shells that form chains, here at 27° to the alignment axis of the nematic host. **B** Schematic of the computational domain. **C** Fully relaxed simulation with $\Gamma_\sigma = 20$, $\Gamma_\kappa = 0$, and $\Gamma_W = 100$, shaded to indicate the relative elastic energy of each mesh face. Two copies of the computational domain are depicted, one reflected about the z axis, to assist visualization.

field in the host nematic, such as spheres with planar anchoring. While far-field theoretical approximations predict chaining angles between 45° and 49° [6, 13, 28, 29], numerical evaluation of the two-dimensional Frank free energy can successfully predict the observed $\sim 30°$ alignment [14]. Additional work has shown that these colloidal interactions depend on shape [30] and size [31] of the particles. Varying the aspect ratios of ellipsoidal particles allows for realization of alignment angles from 30° to 7.5°, and demonstrates that particles with large aspect ratios ($\gtrsim 5$) avoid aggregation [14]. Recently, chaining has also been observed in ferromagnetic nanoparticles [32], although these chaining angles are higher $\sim 54°$ because of shell-shell interactions other than elasticity.

Because no technique can simultaneously resolve the molecular scale order of the liquid crystal and the micron-sized shape of the tactoid, theoretical work requires a trade off between size and resolution. Prior work includes Monte Carlo methods that predict elongation of thermotropic LCs [33] and formation of tetrahedral smectic vesicles [34], Molecular Dynamics simulations that show elongation and spontaneous chiral order in nanoscale droplets [35–38], bead-spring and finite difference models that achieve tactoid elongation on fixed meshes [24, 39, 40], and continuum theory [41, 42] that assumes a rigid idealized shape for the tactoid boundary. Comparing spherical harmonic expansion and finite element methods to predict vesicle shapes, Nguyen et al. found that finite elements handle large deformations well [43]. Finite elements have also been used to simulate defect fields in frustrated geometries [44] or around colloidal spheres [45].

Recently, we created a finite element continuum theory model to determine tactoid shape incorporating a new dynamic mesh control algorithm that ensures the numerical scheme remains accurate and stable during shape minimization [46]. Unlike other finite element schemes used to study soft inclusions in liquid crystals, our scheme incorporates adaptive mesh refinement/coarsening and a moving mesh with regularization to maintain the quality of the representation during large shape changes. Here we will use this strategy to model the shells discussed above.

II. MODEL

The system comprises a nanoparticle shell with nematic liquid crystal on both the interior and exterior. The total free energy,

$$F = F_s + F_n + F_a, \tag{1}$$

includes three contributions: the elastic energy of deforming the shell, the elastic energy of the nematic and an anchoring term that couples the nematic to the shell. The shells are composed of nanoparticles stabilized by ligand-ligand interactions with a short range attraction [12]. These interactions resist changes in the area of the shell. Since the shells are only a few nanoparticles thick, we *a priori* expect the bending energy to be negligible, but include it in the energy to determine its effect on the shape. The shell elastic contribution to (1) is therefore,

$$F_s = \sigma \int_{\partial S} dA + \kappa \int_{\partial S} (H - H_0)^2 \, dA$$

where σ is the surface tension, H is the mean curvature and H_0 is a prescribed mean curvature. We stress that the surface tension σ is intended to capture in an approximate sense *both* the effect of the shell elasticity and the interfacial tension between the shell and the host nematic. We combine these effects because, to linear order, they have the same functional form and neither has been very precisely characterized experimentally for this system. Since these terms depend only on the shell shape and not the director, they do not account for any anisotropic interactions.

Because the shells first form at the interface of an approximately spherical region at a critical radius R, we assume the preferred mean curvature H_0 is that of the

initial sphere ($1/R$). In practice, we find that H_0 and κ have covariant effects on the final shape, so this choice is somewhat arbitrary.

The elastic energy of the LC is the Frank energy [47],

$$F_n = \frac{1}{2}\int_{S,S^\star} dV\Big[K_1(\nabla\cdot\mathbf{n})^2 + K_2(\mathbf{n}\cdot\nabla\times\mathbf{n})^2 + K_3|\mathbf{n}\times\nabla\times\mathbf{n}|^2\Big], \tag{2}$$

where K_1, K_2, and K_3 are the splay, twist, and bend elastic constants, and the integral is taken over the entire simulation volume, i.e. both the interior S and exterior $S^\star$ of the shell. The usual local constraint $\mathbf{n}\cdot\mathbf{n} = 1$ is enforced to ensure the director is a unit vector.

Finally, the anchoring term,

$$F_a = \frac{W}{2}\int_{\partial S} (\mathbf{n}\cdot\hat{\mathbf{s}})^2\, dA, \tag{3}$$

imposes planar-degenerate anchoring relative to the shell surface normal $\hat{\mathbf{s}}$ with associated energy W. Because the shells are ligand-stabilized, we additionally impose a volume constraint,

$$\int_S dV = V_0 \tag{4}$$

We non-dimensionalize the problem by introducing a lengthscale Λ, which we shall later choose to be a typical shell radius, changing variables $x \to \Lambda x'$ and dividing through by $K_1\Lambda/2$. Hence, the energy (1) becomes

$$\frac{F}{K_1\Lambda} = \Gamma_\sigma\int_{\partial S'} dA' + \Gamma_\kappa\int_{\partial S'} (H' - H_0')^2\, dA' + 2F_n'/(K_1\Lambda) + \Gamma_W\int_{\partial S'} (\mathbf{n}\cdot\hat{\mathbf{s}})^2\, dA'. \tag{5}$$

Here we also introduced dimensionless parameters $\Gamma_\sigma = \frac{2\sigma\Lambda}{K_1}$, $\Gamma_\kappa = \frac{2\kappa}{K_1\Lambda}$, and $\Gamma_W = \frac{W\Lambda}{K_1}$, that represent the relative strengths of the surface tension, mean squared curvature, and anchoring energy relative to the elastic energy.

The functional (5) is discretized as follows. First, we exploit the apparent cylindrical symmetry of the shells to work in cylindrical polar coordinates (ρ, ϕ, z). The computational domain, shown in Fig. 1B, is the (ρ, z) plane that must be swept out in ϕ to recover the full 3D solution and is discretized into triangular elements. The initially spherical shell surface is specified as a sequence of edges terminating at top and bottom on the $\rho = 0$ line. The mean curvature H at a given vertex on the shell is calculated using the discrete method from [48]. Director values are stored on each vertex and parametrized in cylindrical coordinates, $\mathbf{n} = (n_\rho, n_\phi, n_z)$ with appropriate derivatives in (2) re-expressed in these coordinates. We emphasize that, in spite of the chosen polar coordinate system, directors may freely rotate out of the (ρ, z) plane. Interpolation of the director between vertices is performed using a special spherical weighted average [49] that maintains unit length at all points. The Frank energy of each element is then computed by gaussian quadrature [50]. The anchoring energy (3) is also computed along the shell by gaussian quadrature.

Having constructed a finite element approximation to (5), we minimize it using gradient descent with respect to both director values and vertex positions from an initial state with $\mathbf{n} = n_z$ at all vertices. To maintain a well-behaved mesh, we supplement the target functional with auxiliary functionals as described in [46] that promote equiangular elements and uniform energy density between adjacent elements. Additionally, local refinement and coarsening is performed to capture adequate detail in regions of high energy density. Fig. 1C shows a converged solution in which the local refinement and energy density reveal the bipolar field adopted by the nematic. The system is considered to have converged when the timestep-normalized percent change to the energy is less than 10^{-6} over two cycles of steps to relax both the vertex location and director orientation. We explicitly test all solutions for stability by computing the bordered Hessian matrix G and testing that the number of constraints plus the number of degrees of freedom for the system is larger than the negative index of inertia plus the corank of G.

III. RESULTS

A. Shell shape

We ran a series of simulations varying the coefficients Γ_σ, Γ_κ and Γ_W to determine how the final shape of the shell depends on these parameters and hence identify the space of accessible shell shapes. We use parameter values for the 5CB host $K_1 = 6.3$ pN, $K_2 = 4.3$ pN, $K_3 = 9.6$ pN [51]. The natural choice for the lengthscale Λ is the shell radius as described earlier; however the experimental results show significant polydispersity. We therefore select the radius of a typical shell and choose $2\Lambda = 6.3$ μm. The explored ranges of the Γ_α correspond to $\sigma = 1$ to 1000 μJ/m^2, $\kappa = 0$ to 10 aJ, and $W = 1$ to 2000 μJ/m^2.

One measure of the final shape is the aspect ratio a, which is displayed in Fig. 2 as a function of surface tension for three values of mean squared curvature strength. The high aspect ratios obtained indicate that the mesh regularization procedure described permits large physical deviations from the initial shape. The inset of Fig. 2C shows a distribution of experimental shell aspect ratios as a function of shell radius. The plot reveals a weak negative trend as might be expected because larger values of Λ effectively increase Γ_σ, resulting in aspect ratios closer to unity regardless of Γ_W and Γ_κ. However, the scatter about this trend is large due to the stochastic nature of the shell formation mechanism.

The simulations reproduce aspect ratios similar to those observed experimentally ($1.0 \le a \le 1.3$) under three different scenarios: first, systems dominated

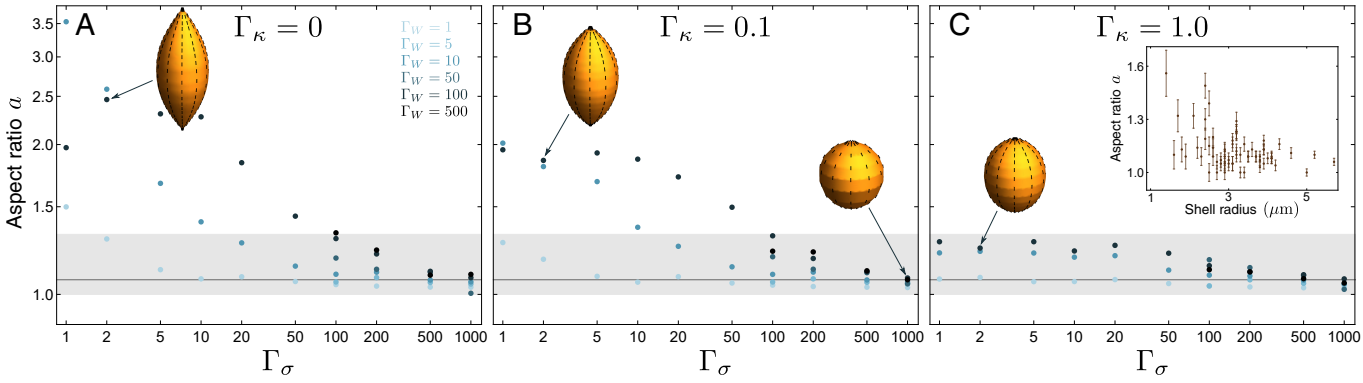

Figure 2. **A-C** Aspect ratio for simulated shells as a function of surface tension for $\Gamma_\kappa = 0$, $\Gamma_\kappa = 0.1$, and $\Gamma_\kappa = 1.0$. The shading of each data point tells the value of Γ_W as indicated by the labels in panel A. The gray region denotes the 90th percentile of the range of aspect ratios observed in the experimental data, with the darker line indicating the median of 1.07. The inset plot in panel C shows the experimental aspect ratios as a function of average shell radius. Inset graphics visualize the shells for selected points with $\Gamma_W = 100$.

by mean squared curvature; second, systems dominated by surface tension; and, third, if the anchoring is very weak. Either of these cases suggests, as we expect, that the interactions between ligands of the nanoparticles are considerably stronger than interactions between LC molecules. Indeed, the experimental shells remain stable even when the surrounding nematic phase is heated to isotropic above 34°C and remain stable up to about 100°C. We address and dismiss the third possibility, systems with very weak anchoring, later on using polarized optical microscopy.

Looking in more detail at the shells displayed in the insets of Fig. 2 there are two distinct morphologies: Surface tension dominated shells form a characteristic cusp at the poles; conversely mean squared curvature dominated shells favor smooth poles. The fluorescence microscopy image shown in Fig. 1A shows evidence of cusps, and so we conclude that the shell elasticity is dominated by surface tension. This is justified by a classic result from shell elasticity: the ratio of bend energy to stretching energy is of order $(R/h)^2$ where R is the shell radius and h is the shell thickness [52]. We estimate the shell thickness to be 10 to 100 times smaller than the radius, which suggests that $\Gamma_\sigma/\Gamma_\kappa$ lies between 100 to 10,000.

Fig. 2 therefore allows us to predict the shapes that would result from changing the experimental system. For example, use of a LC with larger elastic constants would decrease Γ_σ, resulting in more elongated shells. Similarly, decreasing (increasing) the concentration of nanoparticles in the initial system would result in smaller (larger) shells [12], which as discussed above will elongate more (less). The shapes in our system, and their behavior with respect to changing parameters, resemble the those of giant unilamellar vesicles (GUVs) with nematic inside and outside reported in [40] and [24]. However, our shells appear to have a lower bending modulus, as they more readily form cusps without volume loss. Our adaptive moving mesh suits these shells well, as it resolves the shape and field at the cusps of the shells more easily than a fixed finite difference mesh.

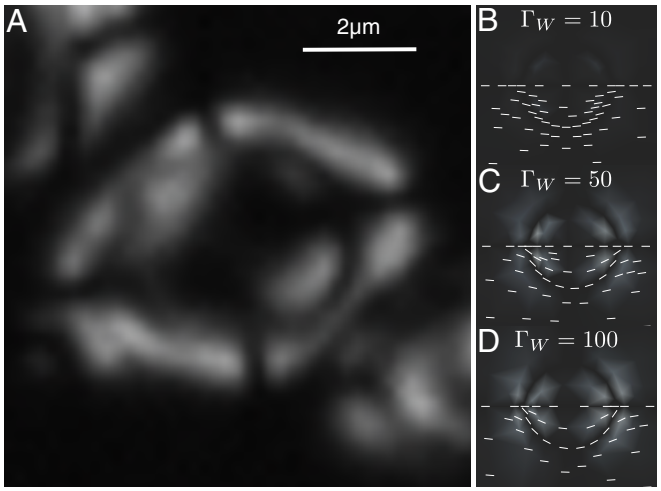

Figure 3. **A** An experimental crossed-polarizer image of a shell imaged close to the central plane. **B-D** Simulated crossed-polarizer images for three shells with different anchoring strengths ($\Gamma_W = 10$, 50, and 100) and aspect ratios equal to the median aspect ratio observed experimentally. The director field superimposed over the simulated images shows stronger anchoring conditions leading to more curvature in the nematic field.

We now turn to the configuration of the liquid crystal around and inside the shell. To facilitate a comparison with experiment, an approximate crossed-polarizer microscope image is generated from each configuration. A very simple optical model is used, treating the LC as a single anisotropic layer in the $y = 0$ plane between two crossed-polarizers above and below the LC. Thus, at a given point the intensity $I = \cos^2\phi \sin^2\phi$, where ϕ is the angle of the director off of the z axis. We emphasize that using a 2D slice is a crude approximation of a true

crossed-polarizer image. Moreover, the optical properties of the NP shell itself are unknown, however motivated by the experimental images, we assume that no light passes through the pixels that lie directly on the shell boundary at $y = 0$.

Results are displayed in panels B through D of Fig. 3 that show simulated microscope images with different anchoring strengths but aspect ratios all within 2% of the median experimental aspect ratio. In spite of the very simple optical model, the simulated images reproduce the main features of the experimental image shown in Fig. 3A: dark bands indicate alignment with one of the polarizers, while bright regions show distortions from a uniform field to match the shell's anchoring preference. The similarity between the two strongest anchoring cases and the experimental image suggests an anchoring parameter of at least $\Gamma_W = 50$. This corresponds to a value of W of order 100 μJ/m^2, consistent with characterizations of strong anchoring [26, 53]. That cases with strong anchoring require $\Gamma_\sigma \geq 500$ to achieve aspect ratios of 1.07 is also consistent with the surface tension-dominated system.

B. Shell-shell interactions and chaining

After formation, the NP shells migrate over the course of minutes to form chains aligned at some angle to the host nematic (Fig. 1A). We measure this angle to be between 25° and 35°, which agrees well with the $\sim 30°$ angles reported by previous studies using particles that produce a quadrupolar distortion field [2, 14, 26, 27, 31]. Mondiot et al. measure a series of angles decreasing below 30° for stiff ellipsoids with increasing aspect ratios and predict these values with a numerical model [14].

Because our shells are non-ellipsoidal, we continue to rely on simulation methods to predict chaining angles. Also, our simulations allow shells to continuously seek out their preferred alignment angles, as opposed to repeated numerical calculations over a range of discrete values. Here, we will adapt the shape evolution technique developed above to include two shells that migrate to locate an equilibrium state. Because the shells composing these chains do not share axes of symmetry, the cylindrical domain above cannot be used. Instead, we develop a two-dimensional model that includes only the projections of the shells onto the $y = 0$ plane.

Minimization of elastic deformations in the host nematic drives the alignment of the shells. However, the results in section III A indicate that these elastic forces are weak compared to the surface tension and anchoring forces that define the shapes of the shells and the LC orientation at the shell-nematic interfaces. Therefore, we fix the shapes of the shells and anchoring conditions, so only the elasticity term of (1) is minimized with respect to the shape of the host nematic domain.

To initialize the simulation, shell shapes and LC director fields at the LC-shell interface are taken from final states of the simulations described in section III A. We place two such shells, offset so that their centers form an angle θ_0 with the z axis, and take gradient descent steps as previously described. As the anchoring of the LC to the shell is fixed, the interior regions of the shells can be excluded from the computational domain.

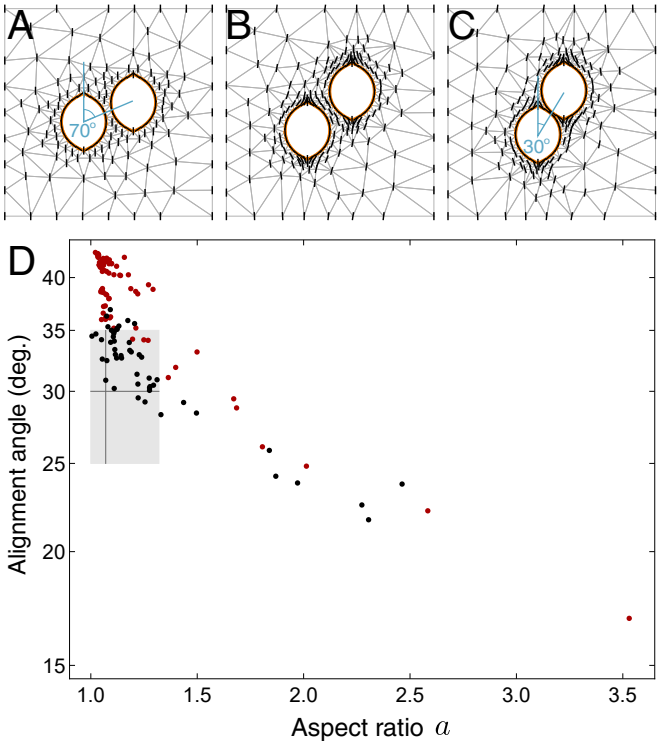

Figure 4. **A-C** Simulation snapshots of two shells with aspect ratio = 1.18 relaxing from $\theta_0 = 70°$ to $\theta_p = 30°$. The shells repel initially, before finding their preferred alignment angle and attracting one another. **D** Preferred alignment angle θ_p as a function of shell aspect ratio for all of the simulated cases shown in Fig. 2. The black series contains cases with strong anchoring ($\Gamma_W \geq 50$) while the red series contains cases with weaker anchoring ($\Gamma_W < 50$). The gray region denotes the range of aspect ratios and angles observed in the experimental data, with the darker lines indicating the medians of 1.07 and 30°.

Results from a typical run are shown in Fig. 4. Panels A through C show selected snapshots from a simulation where the starting alignment angle $\theta_0 = 70°$. Initially, the shells repel each other, before rotating around to find a preferable angle and then collapsing together. This behavior of repulsion at angles close to 0° or 90° and attraction at intermediate angles is well-documented experimentally [26, 27].

Fig. 4D displays the simulated chaining angle as a function of the aspect ratio of the NP shells with strong (black) and weak (red) anchoring. As aspect ratio increases, the chaining angle is reduced. Noise in the plot is due to variations in the anchoring condition and bend modulus from the initial configuration. For shells with aspect ratios in the range observed experimentally, we

see preferred angles mostly from 28° to 36°, which is in very good agreement with the chains seen experimentally. Furthermore, extrapolation of the strong anchoring data in the limit of $a \to 1$, i.e. spherical colloidal particles with rigid anchoring, implies $\theta_p = 34°$, which agrees well with the 30° reported by other authors.

Compared to Fig. 4D, [14] shows a similar trend but finds a steeper slope. This is expected because our sharply-pointed shells mimic the curvature of lower aspect ratio ellipsoids away from the shell cusps. In fact, shell bending modulus could be tuned to select the desired regime of alignment angles for a given shell aspect ratio.

The results presented agree with previous studies of analogous systems, but represent a significant relaxation of the assumptions inherent in such models. Ideally, one would minimize Eq. (5) in 3D with respect to arbitrary variations of **n**, the shell shapes and positions. Of the previous studies on chaining of which we are aware, only one 3D model [31] uses non-spherical particles (spherocylinders) of fixed shape, while all other non-spherical shapes are simulated with 2D models [14] and [39]. None of these existing studies (2D or 3D) consider shells of arbitrary shape, or allows the shape to vary. Our approach is readily generalized to 3D, a topic of future work.

IV. CONCLUSION

We present a continuum theory finite element model for deformation and two body interactions of flexible shells in a nematic liquid crystal. The model features dynamic mesh remodeling utilizing auxiliary functionals to maintain accuracy despite large deformations from the initial configuration. The model is used to simulate experimentally observed elongation and chaining of mesogen-functionalized nanoparticle shells that form as LCs are quenched into the nematic phase. Because the elastic behavior of these shells is unknown, the model enables us to extract the contributions of shell elasticity, nematic elasticity and anchoring from the observed shapes. By comparing simulations with experimental images, we determine surface tension and anchoring dominate the system.

Extending the model to incorporate multiple shells, we predict the chaining angles attained by the shells, and determine the dependence of chaining angle on shell aspect ratio, which matches within reason previous results reported on a similar system. Furthermore, our model predicts the chaining angle of spherical particles with strong planar anchoring in a nematic LC more accurately than far-field theoretical treatments.

Our simulations cover a wide range of parameter space, so information from these results enables us to design systems with particular shell sizes, shapes, and alignment angles. This ability to control and tune particle shape by a scalable self-assembly method is valuable as part of designing hierarchical processes. Furthermore, the simulation methodology presented is computationally cheap and readily adapted, with little modification, to a wide variety of shape-order problems involving soft materials.

We caution that the NP shells in a nematic background presented in this paper differ considerably from nematic shells in a double emulsion [54–56]. Possessing two nematic-water interfaces with strong surface tension, these shells do not tend to deform, and owing to the isolated nematic region composing each shell, more elaborate defect structures often form. However, future model applications include nematic shells, as well as other systems in which a nematic background surrounds a thin elastic shell such as a domain wall or defect loop. Furthermore, the variable-domain nature of our model makes it well-suited to investigate phase transition and shear flow phenomena in liquid crystals. Lastly, deformation results given by the model could be compared with theoretical approximations that attempt to capture large deformations [57].

ACKNOWLEDGMENTS

ADB is supported by a Tufts University Burlingame Fellowship. TJA acknowledges support from the National Science Foundation under grant no. DMR-CMMT-1654283. *TJA is also supported by a Cottrell Award from the Research Corporation for Science Advancement. LSH and ALR acknowledge financial support from the National Science Foundation grant no.* DMR-CBET-1507551. *This work was partly performed at the Aspen Center for Physics, which is supported by National Science Foundation grant* PHY-1066293.

[1] S. P. Meeker, W. C. K. Poon, J. Crain, and E. M. Terentjev, Phys. Rev. E **61**, R6083 (2000).
[2] I. Muševič, M. Škarabot, U. Tkalec, M. Ravnik, and S. Žumer, Science **313**, 954 (2006).
[3] I.-H. Lin, G. M. Koenig, J. J. de Pablo, and N. L. Abbott, The Journal of Physical Chemistry B **112**, 16552 (2008).
[4] G. M. Koenig, I.-H. Lin, and N. L. Abbott, Proceedings of the National Academy of Sciences **107**, 3998 (2010).
[5] P. Poulin, H. Stark, T. C. Lubensky, and D. A. Weitz, Science **275**, 1770 (1997).
[6] P. Poulin and D. A. Weitz, Phys. Rev. E **57**, 626 (1998).
[7] M. Škarabot, M. Ravnik, S. Žumer, U. Tkalec, I. Poberaj, D. Babič, N. Osterman, and I. Muševič, Phys. Rev. E **77**, 031705 (2008).
[8] J. Milette, S. J. Cowling, V. Toader, C. Lavigne, I. M. Saez, R. Bruce Lennox, J. W. Goodby, and L. Reven, Soft Matter **8**, 173 (2012).

[9] A. L. Rodarte, R. J. Pandolfi, S. Ghosh, and L. S. Hirst, J. Mater. Chem. C **1**, 5527 (2013).

[10] J. B. Miller, A. C. P. Usselman, R. J. Anthony, U. R. Kortshagen, A. J. Wagner, A. R. Denton, and E. K. Hobbie, Soft Matter **10**, 1665 (2014).

[11] H. Wu, L. X. Chen, X. Q. Zeng, T. H. Ren, and W. H. Briscoe, Soft Matter **10**, 5243 (2014).

[12] A. L. Rodarte, B. H. Cao, H. Panesar, R. J. Pandolfi, M. Quint, L. Edwards, S. Ghosh, J. E. Hein, and L. S. Hirst, Soft Matter **11**, 1701 (2015).

[13] H. Stark, Physics Reports **351**, 387 (2001).

[14] F. Mondiot, S. Prathap Chandran, O. Mondain-Monval, and J.-C. Loudet, Phys. Rev. Lett. **103**, 238303 (2009).

[15] P. Rofouie, D. Pasini, and A. D. Rey, Soft Matter , (2017).

[16] V. H. Zocher, Zeitschrift für Anorg. und Allg. Chemie **147**, 91 (1925).

[17] V. H. Zocher and K. Jacobsohn, Kolloid Beih. **28**, 167 (1929).

[18] J. D. Bernal and I. Fankuchen, J. Gen. Physiol. **25**, 111 (1941).

[19] C. Casagrande, P. Fabre, M. A. Guedeau, and M. Veyssie, Europhys. Lett. **3**, 73 (1987).

[20] Y.-K. Kim, S. V. Shiyanovskii, and O. D. Lavrentovich, J. Phys. Condens. Matter **25**, 404202 (2013).

[21] S. Zhou, K. Neupane, Y. A. Nastishin, A. R. Baldwin, S. V. Shiyanovskii, O. D. Lavrentovich, and S. Sprunt, Soft Matter **10**, 6571 (2014).

[22] V. Jamali, N. Behabtu, B. Senyuk, J. A. Lee, I. I. Smalyukh, P. van der Schoot, and M. Pasquali, Phys. Rev. E **91**, 042507 (2015).

[23] P. C. Mushenheim, R. R. Trivedi, D. B. Weibel, and N. L. Abbott, Biophys. J. **107**, 255 (2014).

[24] R. Zhang, Y. Zhou, J. A. Martínez-González, J. P. Hernández-Ortiz, N. L. Abbott, and J. J. de Pablo, Sci. Adv. **2** (2016).

[25] F. C. Keber, E. Loiseau, T. Sanchez, S. J. DeCamp, L. Giomi, M. J. Bowick, M. C. Marchetti, Z. Dogic, and A. R. Bausch, Science **345**, 1135 (2014).

[26] R. W. Ruhwandl and E. M. Terentjev, Phys. Rev. E **55**, 2958 (1997).

[27] I. I. Smalyukh, O. D. Lavrentovich, A. N. Kuzmin, A. V. Kachynski, and P. N. Prasad, Phys. Rev. Lett. **95**, 157801 (2005).

[28] S. Ramaswamy, R. Nityananda, V. A. Raghunathan, and J. Prost, Molecular Crystals and Liquid Crystals Science and Technology. Section A. Molecular Crystals and Liquid Crystals **288**, 175 (1996).

[29] T. Araki and H. Tanaka, Phys. Rev. Lett. **97**, 127801 (2006).

[30] C. P. Lapointe, T. G. Mason, and I. I. Smalyukh, Science **326**, 1083 (2009).

[31] F. R. Hung, Phys. Rev. E **79**, 021705 (2009).

[32] I. Dierking, M. Heberle, M. Osipov, and F. Giesselmann, Soft Matter (2017).

[33] M. A. Bates, Chem. Phys. Lett. **368**, 87 (2003).

[34] X. Xing, H. Shin, M. J. Bowick, Z. Yao, L. Jia, and M.-H. Li, Proc. Natl. Acad. Sci. U. S. A. **109**, 5202 (2012).

[35] M. Tsige, M. P. Mahajan, C. Rosenblatt, and P. L. Taylor, Phys. Rev. E **60**, 638 (1999).

[36] R. Berardi, A. Costantini, L. Muccioli, S. Orlandi, and C. Zannoni, The Journal of Chemical Physics **126**, 044905 (2007).

[37] L. F. Rull, J. M. Romero-Enrique, and A. Fernandez-Nieves, The Journal of Chemical Physics **137**, 034505 (2012).

[38] D. Vanzo, M. Ricci, R. Berardi, and C. Zannoni, Soft Matter **8**, 11790 (2012).

[39] F. E. Mackay and C. Denniston, Soft Matter **9**, 5285 (2013).

[40] P. C. Mushenheim, J. S. Pendery, D. B. Weibel, S. E. Spagnolie, and N. L. Abbott, Proc. Natl. Acad. Sci. U. S. A. **113**, 5564 (2016).

[41] A. V. Kaznacheev, M. M. Bogdanov, and S. A. Taraskin, J. Exp. Theor. Phys. **95**, 57 (2002).

[42] P. Prinsen and P. Van Der Schoot, Eur. Phys. J. E **13**, 35 (2004).

[43] T.-S. Nguyen, J. Geng, R. L. B. Selinger, and J. V. Selinger, Soft Matter **9**, 8314 (2013).

[44] R. H. Nochetto, S. W. Walker, and W. Zhang, SIAM J. Numer. Anal. **55**, 1357 (2017).

[45] I. Bajc, F. Hecht, and S. Åœumer, J. Comput. Phys. **321**, 981 (2016).

[46] A. DeBenedictis and T. J. Atherton, Liquid Crystals **43**, 2352 (2016).

[47] F. C. Frank, Discuss. Faraday Soc. **25**, 19 (1958).

[48] N. Dyn, K. Hormann, S.-J. Kim, and D. Levin (Vanderbilt University, Nashville, TN, USA, 2001) Chap. Optimizing 3D Triangulations Using Discrete Curvature Analysis, pp. 135–146.

[49] S. R. Buss and J. P. Fillmore, ACM Transactions on Graphics (TOG) **20**, 95 (2001).

[50] D. A. Dunavant, International Journal for Numerical Methods in Engineering **21**, 1129 (1985).

[51] E. Nowinowski-Kruszelnicki, J. Kędzierski, Z. Raszewski, L. Jaroszewicz, M. A. Kojdecki, W. Piecek, P. Perkowski, M. Olifierczuk, E. Miszczyk, K. Ogrodnik, and P. Morawiak, Opto-Electron. Rev. **20**, 255 (2012).

[52] L. D. Landau, L. P. Pitaevskii, A. M. Kosevich, and E. M. Lifshitz, "Theory of elasticity," (2012).

[53] O. V. Kuksenok, R. W. Ruhwandl, S. V. Shiyanovskii, and E. M. Terentjev, Phys. Rev. E **54**, 5198 (1996).

[54] A. Fernández-Nieves, V. Vitelli, A. S. Utada, D. R. Link, M. Márquez, D. R. Nelson, and D. A. Weitz, Phys. Rev. Lett. **99**, 157801 (2007).

[55] T. Lopez-Leon, V. Koning, K. Devaiah, V. Vitelli, and A. Fernandez-Nieves, Nat. Phys. **7**, 391 (2011).

[56] H.-L. Liang, S. Schymura, P. Rudquist, and J. Lagerwall, Phys. Rev. Lett. **106**, 247801 (2011).

[57] J. Gielis, Am. J. Bot. **90**, 333 (2003).